Charge control of micro-particles in a shielded plasma afterglow

Document license:
TAVERNE

DOI:
[10.1088/1361-6595/ab8e4f](10.1088/1361-6595/ab8e4f)

Document status and date:
Published: 09/06/2020

Document Version:
Publisher's PDF, also known as Version of Record (includes final page, issue and volume numbers)

Please check the document version of this publication:

• A submitted manuscript is the version of the article upon submission and before peer-review. There can be important differences between the submitted version and the official published version of record. People interested in the research are advised to contact the author for the final version of the publication, or visit the DOI to the publisher's website.
• The final author version and the galley proof are versions of the publication after peer review.
• The final published version features the final layout of the paper including the volume, issue and page numbers.

Link to publication

PAPER

Charge control of micro-particles in a shielded plasma afterglow

View the article online for updates and enhancements.

Charge control of micro-particles in a shielded plasma afterglow

B van Minderhout[1,3] , **J C A van Huijstee**[1] , **B Platier**[1] , **T Peijnenburg**[2],
P Blom[2], **G M W Kroesen**[1] **and J Beckers**[1]

[1] Department of Applied Physics, Eindhoven University of Technology, PO Box 513, 5600 MB
Eindhoven, The Netherlands
[2] VDL Enabling Technologies Group, PO Box 80038, 5600 JW Eindhoven, The Netherlands

E-mail: b.v.minderhout@tue.nl

Abstract
In this work, charge control of micro-particles from ~-40 to $+10$ elementary charges is
presented. This is achieved at 0.9 mbar argon in the spatial afterglow of an inductively coupled
plasma by solely changing the strength of an externally applied electric field. Crucial in the
presented experiments is the use of a grounded mesh grid in the cross section of the setup,
separating the active plasma region from the 'shielded' spatial afterglow. While in the regions
above the mesh grid all particles reached a constant negative equilibrium charge, the actual
control achieved in the shielded spatial afterglow can most probably be explained by variations
of the local ion density. The achieved charge control not only opens up possibilities to study
nano-scale surface charging physics on micro-meter length scales, it also contributes to the
further development of plasma-based contamination control for ultra-clean low-pressure
systems.

Keywords: plasma-assisted contamination control, complex plasma, spatial afterglow, particle
charge control

(Some figures may appear in colour only in the online journal)

1. Introduction

In dusty or complex plasmas, i.e. plasmas containing nano-
to micro-meter sized particles, the plasma-induced particle
surface charge is known to be one of the key parameters
driving elementary processes such as ion drag [1, 2], local
Debye shielding [3], Coulomb-interactions in strongly cou-
pled plasmas [4] and plasma-particle synthesis [5]. In the
latter example, the particle charge is especially important
in the particle coagulation step [6, 7]. In the bulk of a
plasma, micro-particles typically reach a permanent nega-
tive charge of $(10^3$ to $10^4)$ elementary charges [8]. This is
because the particle charge is determined by the balance of
ion and electron fluxes reaching the surface of the parti-
cle. Since the electrons are much more mobile than ions,
an equilibrium in flux is achieved for a negative surface
potential.

In the region where the plasma is not actively powered, i.e.
the plasma afterglow, the typical charge of particles is signifi-
cantly lower than in the plasma bulk [9–11]. The evolution of
the particle charge differs for temporal and spatial afterglows.
Where in the temporal afterglow the charge is determined by
the plasma changes in time [10–17], in the largely unexplored
spatial afterglow, the particle charge is determined by the spa-
tial evolution of plasma parameters, such as the electron tem-
perature and the plasma density. In the case of the temporal
afterglow, it is known in literature that a dc field can influ-
ence the particle charge. Wörner *et al* [18] have experimentally
shown that a dc field can shift the charge distribution of micro-
particles from a negative to a positive mean value at high dust
densities. The authors studied this effect for a single dc electric
field strength. In addition, Couëdel *et al* have shown that the
particle charge is determined by the manner in which the tran-
sition from ambipolar to free diffusion takes place [14]. In any
case, it is difficult to control the particle charge in the plasma
afterglow. Yet, particle charge control opens up a wide variety

---

[3] Author to whom any correspondence should be addressed.

of opportunities both from a fundamental and an application perspective.

Fundamentally, charge control of micro-particles allows to study nano-scale surface physics on micro-meter length scales. Examples of relevant processes are photodetachment [19], photoionisation [20], charge attachment [21, 22] and secondary electron emission [23]. From an application point of view, charge control of particles could improve the properties and deposition of silicon nano-crystals, which are synthesised in reactive plasmas [24] for the creation of nano-devices.

In addition, particle contamination becomes an increasingly significant problem in many ultra-clean low-pressure systems, for instance in the multi-billion-dollar semiconductor industry [25]. Charge control in this situation is an important step in enabling *in situ* particle contamination control [9]. The principle of such a plasma-assisted particle mitigation technique is based on the ability of plasma to both electrically charge the contaminating particles and to affect the trajectories by the plasma-induced electric fields [26].

Because the mentioned fundamental opportunities and applications have high potential, carefully controlling the charge of these particles is crucial. This has been far from trivial until now, which is illustrated by the following three examples.

First of all, it is virtually impossible to generate or directly inject neutral particles in a system because of the triboelectric effect [27]. Consequently, a charge control technique must be able to reset the triboelectrically induced charge distribution, which includes both positively and negatively charged particles [28].

Secondly, Bennet *et al* have reported a multi-step charge control process [29]. In this process, first, the micro-particle was encapsulated in a water droplet, then the droplet was charged in a plasma discharge. Afterwards, the droplet was evaporated outside the plasma until the Rayleigh limit was reached. The authors have claimed that when the droplet collapsed a precise amount of charge was delivered to the particle because of this Rayleigh limit. This example shows that controlling the charge of micro-particles is a complex and multi-step process in which one has to deal with plasma afterglow effects and water vapour contamination, for instance.

Thirdly, the PK4 experiment has the ability to carefully alter the particle charge in the active plasma region [30, 31]. While the control of the micro-particle charge in the latter experiment was achieved by varying the pressure, these variations in pressure also changed the drift velocity and the position of the particles.

The three examples described above show not only that plasma is needed to reset the initial charge of the particles but also that a complicated multi-step process is required to get a precise amount of charge on micro-particles outside the active plasma region.

In previous work we measured the particle charge in the free spatial afterglow [9], i.e. without application of a mesh grid. In that paper we have shown that the charge in the free

afterglow is significantly lower than the charge in the plasma bulk which served as a proof of principle of our measurement technique. In this paper, we introduce a plasma-based method to control the charge of micro-particles around zero ($\sim -40e$ to $+10e$) by the application of a grounded mesh grid and by variation of a dc electric field below and towards the mesh grid. The applied electric field in this work changes the local ion density in the shielded spatial afterglow, thereby allowing charge control over particles with both positive and negative charges. The strength of this technique is that it involves only a one-step process.

In the next sections of this paper, we will first discuss the particle charging theory (section 2) and subsequently introduce the experimental setup and diagnostics used in section 3. Special focus will be on the key variable in the presented method, i.e. the externally applied electric field. Then, the proof of principle of our charge control method is presented in section 4. The physical interpretation is elaborated in section 5 which is divided in the three defined regions of our experiment: the active plasma region, the sheath above the mesh grid and the shielded plasma afterglow, where the actual charge control is achieved.

2. Particle charging theory

As explained in the introduction, dust particles generally acquire a negative charge in a low-pressure plasma [8]. The acquired charge is in most cases described by the orbital motion limited (OML) theory [8, 32]. In this theory, the plasma sheath around the particle is assumed to be collisionless and furthermore it is assumed that ions and electrons are collected by the particle when their orbits overlap. OML theory can be applied only as long as the particle radius $r_p \ll \lambda_D$, where λ_D is the Debye length, the smallest length scale on which plasma parameters can be considered constant.

For an isolated particle in a plasma with Maxwellian electrons and exclusively positive ions, the ion current I_i and the electron current I_e collected by the particle can be expressed as [33]

$$
I_{i,e} =
\begin{cases}
I_{i0,e0}\left(1 - \dfrac{q_{i,e}\phi_s}{k_B T_{i,e}}\right) & \text{if } q_{i,e}\phi_s \leqslant 0 \\[2ex]
I_{i0,e0} \exp\left\{-\dfrac{q_{i,e}\phi_s}{k_B T_{i,e}}\right\} & \text{if } q_{i,e}\phi_s \geqslant 0.
\end{cases}
\tag{1}
$$

As can be seen, the ion and electron current depend on the surface potential of the particle ϕ_s as well as on the charge $q_{i,e}$ and the temperature $T_{i,e}$ of the ions and the electrons. Furthermore, in equation (1), k_B is the Boltzmann constant and $I_{i0,e0}$ is the current collected at $\phi_s = 0$. By solving the current balance $I_i = I_e$, the particle charge Q can be derived for a spherical particle according to

$$
Q = 4\pi\epsilon_0\epsilon_r r_p \phi_s
\tag{2}
$$

where ϵ_0 and ϵ_r are the vacuum and relative permittivities, respectively.

At the pressure used in this work, $p = 0.9$ mbar argon, the plasma sheath (around the particle) is not collisionless and

therefore the ion current is in fact altered by ion-neutral collisions. Yet, these collisional effects only change the particle charge in the plasma bulk by a factor three at maximum [1, 34] and therefore collisional effects are omitted in the analysis in this work.

The particle charging timescale τ_c, which is the characteristic timescale a particle needs to reach its equilibrium charge in a plasma, can be derived from OML theory. For the usual situation in a low-pressure plasma where $T_e \gg T_i$ the charging timescale τ_c is given by [35]

$$\tau_c = \frac{4\epsilon_0}{e^2} \sqrt{\frac{k_B T_i \pi m_i}{8}} \frac{1}{r_p n_{e,i}(1 + y_0)}. \qquad (3)$$

Here, e is the elementary charge of an electron, m_i the ion mass and y_0 the equilibrium value of the reduced particle potential $y = e\phi_s / k_B T_e$.

3. Experimental setup

In this section the experimental setup and the particle diagnostic are presented. The next paragraph briefly introduces the main elements of the plasma particle charging investigation (PPCI) setup [9], after which the most relevant parts will be elaborated in separate subsections moving from the top to the bottom of the setup.

The PPCI setup is a vacuum system consisting of a 1 m glass tube with a base pressure of roughly 5×10^{-7} mbar. A sketch of the PPCI setup is shown in figure 1. In order to increase the accuracy of the charge measurements and to simplify the analysis, a square cross-sectional shape was chosen for the tube with an inner width of $D = 0.1$ m. At the top of the glass tube a shower head was mounted through which gas and particles were injected. After injection, these particles fell through an inductively coupled plasma (ICP) which was generated using a five-turn square coil wound around the outside of the tube. This active plasma region was shielded from the remainder of the setup by a grounded metal mesh grid in the cross section of the tube downstream of the ICP. In the shielded spatial afterglow below the mesh grid, the charge control of the particles was verified by measuring the position, velocity and acceleration of these particles in an externally applied electric field created by two Rogowski electrodes [36]. During their fall through the entire setup, the particles were illuminated with a laser system and their scattered light was recorded by a high-speed camera.

3.1. Particle and gas injection

At the top of the PPCI setup particle and gas injection were combined in the showerhead. The micro-particles, supplied by microParticles GmbH, consisted of a melamine formaldehyde (MF) core and a porous silver coating with a thickness of ~100 nm to minimize triboelectric charging effects [27]. These particles, with a diameter (4.9 ± 0.2) μm and (supplier provided) particle mass of $m_p = 9 \times 10^{-14}$ kg, were injected using a particle dispenser similar to those used in earlier studies [28, 37]. After injection, the particles left the showerhead at its centre through a 5 mm thick and 40 mm wide slit. On the
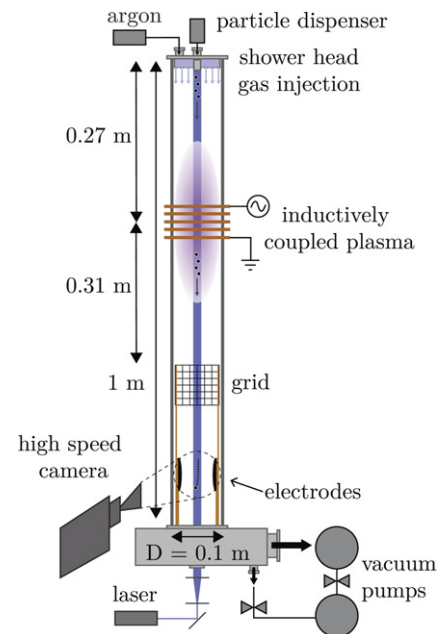

Figure 1. Schematic drawing of the PPCI setup in which micro-particles fell through a spatially limited region of plasma after which their charge was measured by accelerating them in an externally applied electric field. In this paper the spatial afterglow was shielded from the active plasma region by a grounded mesh grid.

one hand this slit ensured that particles were injected into a defined volume matching the laser sheet dimensions and on the other hand the slit served as a beam dump for the laser. The 10 sccm argon flow, regulated with a Brooks SLA850 mass flow controller, was distributed over the entire cross-section of the tube through ≈200 holes of 0.5 mm in diameter equally distributed around the slit. In this manner, the flow entrance effects were reduced and stable particle injection was ensured. In addition, the flow together with gravity accelerated the particles to a measured settling velocity $v_{p,f} = 0.13$ ms^{-1}.

3.2. Active plasma region

By sending a radiofrequent (RF) current at 13.56 MHz through a five-turn square coil wound around the outside of the tube, an ICP was created inside the tube. The RF signal was generated with an Agilent 33220A function generator, amplified by an E & I AB250 power amplifier and matched with a T-matching circuit to convert the complex plasma impedance at 13.56 MHz to a 50 Ω resistive load seen by the amplifier. Taking the centre of the coil as a reference, the coil was placed 0.27 m under the showerhead and 0.31 m above the grounded mesh grid. This mesh grid limited the active plasma region in volume and created the spatial afterglow region downstream. The region below the mesh grid will be referred to in this paper as the shielded spatial afterglow and is the main interest in this work.

The wires of the mesh grid had a diameter of 0.37 mm and the distance between two wires was 1.13 mm. Because of the presence of the mesh grid, the plasma was mainly capacitively coupled, which was supported by the plasma density measured using the Microwave Interferometer MWI 2650.
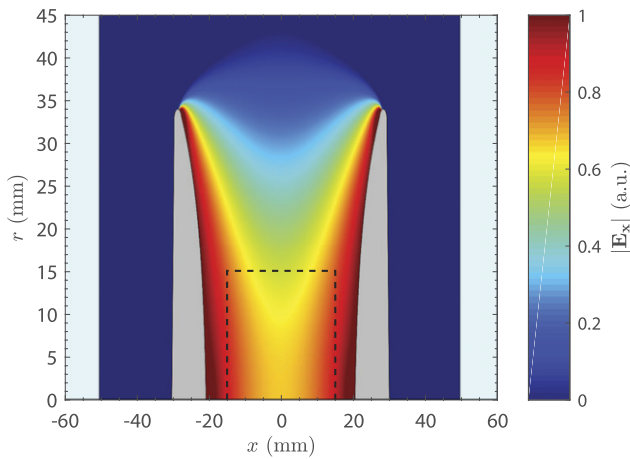
Figure 2. Normalised horizontal component of the electric field created between the Rogowski electrodes. The electrodes are indicated in grey and the glass tube in light blue. Cylindrical geometry is used which implies that the front and back glass plate of the tube are not taken into account in the simulation. A potential difference of 300 V is applied between the electrodes.
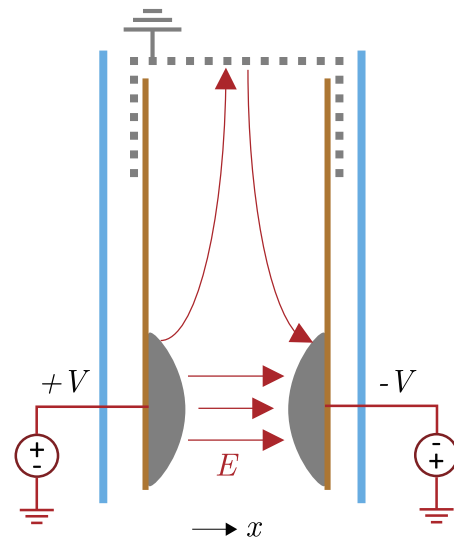

Figure 3. Sketch of the field lines present in the shielded spatial afterglow of the PPCI setup. Indicated in blue are the walls of the glass tube, in brown the peek (polyetheretherketone) stands that support the electrodes and the mesh grid, and in red the field lines. The potential is applied to the electrodes using two power supplies.

This MWI system had an operating frequency of 26.5 GHz and was used and described in previous research [38, 39]. The measured density 26 mm above the mesh grid, obtained using extrapolation and without sheath path length correction, was $n_{e,i} \approx 10^{14}\,\mathrm{m}^{-3}$. The measured value of $n_{e,i}$ corresponds to the E-mode of ICPs [40] which is the capacitive mode. The main message here is that the plasma was mainly capacitively coupled because of the presence of the mesh grid. In this manner, 6 W of power was delivered to the plasma volume at an argon pressure of $p = 0.9\,\mathrm{mbar}$.

3.3. Rogowski electrodes

The plasma-induced charge of the micro-particles was measured by accelerating them in an externally applied dc electric field directed perpendicular to the settling velocity vector of the particles. This field was created by applying a voltage difference between two Rogowski electrodes [36]. The curved shape of these electrodes suppressed the field enhancement near the edges of the electrodes, which increased the maximum electric field that could be applied in the central region of the electrodes without creating a dc glow discharge. The Rogowski electrodes were 70 mm in diameter and had a separation distance of 40 mm. A 2D electrostatic model was set up in COMSOL to obtain the electric field profile which is shown in figure 2. From this figure it follows that the horizontal field strength in the central region 30×30 mm between the Rogowski electrodes (indicated in figure 2 by dashed lines) differed at max 30%. Consequently, the electric field was considered to be constant in this region.

The breakdown electric field between the electrodes was experimentally measured to be $E_{bd} = 8\,\mathrm{kV\,m^{-1}}$ while the ICP was ignited. The maximum electric field used in the experiments was $5\,\mathrm{kV\,m^{-1}}$, far below E_{bd}. Therefore, possible reionization has a negligible effect on the particle charge.

In addition to the field between the electrodes, the presence of the grounded mesh grid also created a field above the electrodes both in horizontal and vertical direction. In figure 3 field lines are sketched which visualize these field components.

Using a trans impedance amplifier (TIA), the AccTec electrometer 2, the anode and cathode currents to ground were measured to analyse the electron and ion current received by the electrodes. The configuration in which these experiments were performed is schematically depicted in figure 4. In order to suppress the RF noise, a low-pass RC-filter was applied with a cut-off frequency of 100 kHz. In addition, the current measurements were performed in a floating configuration, i.e. the oscilloscope (Agilent DSO-X 2020A) and the TIA were not grounded, as indicated in figure 4. In order to increase the accuracy of the current measurements, the TIA was read out by an oscilloscope over a period of 2 s with a sampling frequency of 25 kHz. Subsequently, the average current was used in the further analysis. It will be shown in the results section that the electrodes have a crucial role in the particle charge control, in addition to their importance for the charge measurement.

3.4. Particle trajectory imaging

The trajectories of the particles were visualised within the imaging window by laser light scattering. To this end, a diode laser with a central wavelength of 447 nm was used together with collimation optics and cylindrical lenses to create a 3 mm thick and 40 mm wide laser sheet. This laser sheet was directed antiparallel to the direction of the settling velocity of the particles (see figure 1). The scattered laser light was imaged by a Photron Fastcam mini UX100 high speed camera at 1000 fps, with its viewing direction perpendicular to the plane of the laser sheet. It is the 3 mm thickness of this laser sheet which assured that particles moving towards or away
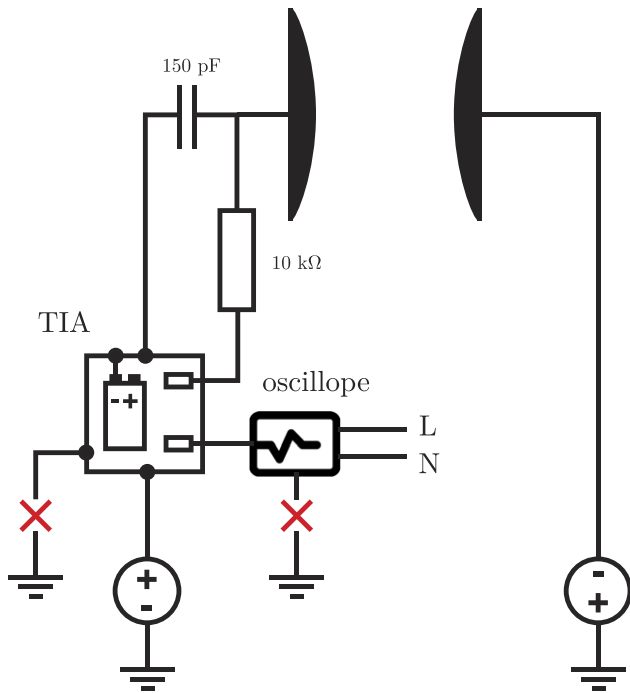
Figure 4. Sketch of the electrical configuration in which the cathode and anode current to ground have been measured. The trans impedance amplifier (TIA) and the oscilloscope are both not grounded.
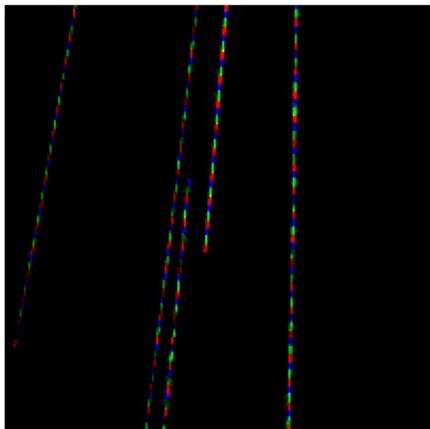

Figure 5. Typical raw image of particles falling in the region between the electrodes. 54 frames are subsequently coloured red, green and blue indicating the movement of the particles. The images are recorded in grey scale at 1000 fps. The representation shows a zoomed part (6 × 6 mm) of the total field of view.

from the camera, i.e. particles that were moving parallel to the viewing direction of the camera, were only shortly imaged and thereby omitted in the analysis. A representation of the typical raw data of the measured particle trajectories is shown in figure 5. This image clearly shows that the particle density in our experiments is low.

The field of view (FoV) of the camera was approximately 40 mm in horizontal direction and 32 mm in vertical direction, where the particles were only detected in the central 30 mm in horizontal direction (see figure 10). Consequently, 1 pixel

corresponded to roughly 32 μm which is much larger than the diameter of the micro-particles. In order to increase the particle detection accuracy, the optics were slightly put out of focus on purpose. In this manner, the particles were detected on multiple pixels and consequently their positions could be determined at sub-pixel accuracy.

3.5. In-house developed particle tracking software

In order to obtain information about the charge of the micro-particles, their horizontal velocity and acceleration were obtained from the recorded trajectories using in-house developed particle tracking software written in Matlab. The analysis consisted of a three-step process.

First of all, the positions of all particles in each frame were determined. Using morphological operations a mask was generated that located the positions of all particles. The exact location of each particle detection was determined by calculation of its intensity weighted midpoint. Here, it was important that each particle detection consisted of multiple pixels which was achieved by deliberately placing the optics slightly out of focus (see section 3.4). In this way, the particle positions were determined in each frame with an accuracy of about 5 μm.

Second, these individual particle positions were linked in order to create trajectories. For the particles detected at the top of the frames a new trajectory was started. For all other particle positions the cost (the difference between the measured and expected particle position) was calculated to assign the detections to each existing trajectory. In this way, a cost matrix was created and subsequently solved by finding the lowest total linking cost. Thereby, all positions in one frame were simultaneously assigned to the existing trajectories or new trajectories were started. In more detail, the linking cost was determined by the difference between the Kalman filter's prediction of the next position of the trajectory and the particle detections. The cost matrix was solved using the Hungarian assignment algorithm.

Third, the trajectories were quadratically fitted and their horizontal velocity and acceleration (anti-)parallel to the externally applied electric field amongst other parameters were obtained. In this manner, the determined velocity was the initial velocity with which particles entered the field of view and the acceleration the change in velocity within this region. The locally obtained acceleration is not the local derivative of the velocity.

3.6. Charge measurement

In previous work [9] the charge, in the free afterglow in the same configuration but without grid, was obtained from the horizontal acceleration which the residually charged particles experienced in the region of externally applied electric field. The particle charge in this work is instead based on the horizontal velocity. While the horizontal acceleration of the small particle charges was not much larger than the flow disturbances, the horizontal velocity showed the integrated effect of the electric field in the region above the field of view. The flow
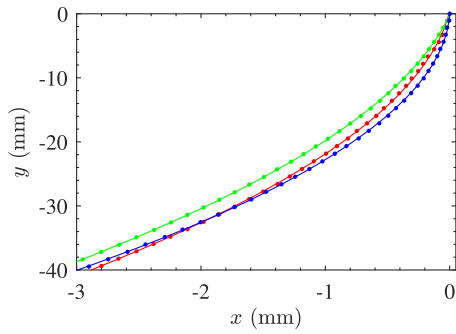
Figure 6. Three typical particle trajectories together with a quadratic fit in the region of an externally applied electric field ($E = 4.3 \, \text{kV m}^{-1}$) in the free spatial afterglow [9]. Every tenth data point is plotted for clarity. In addition, the starting point of each trajectory is transformed to the origin.
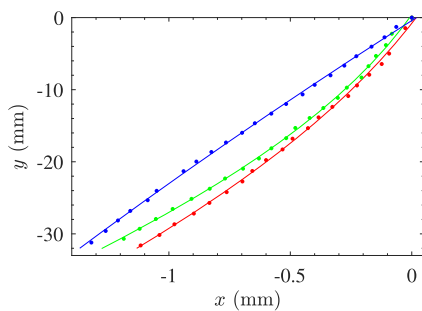

Figure 7. Three typical particle trajectories together with a quadratic fit in the region of an externally applied electric field in shielded spatial afterglow for $E = 1.25 \, \text{kV m}^{-1}$. Every tenth data point is plotted for clarity. In addition, the starting point of each trajectory is transformed to the origin.

Figure 8. Horizontal velocity v_x as a function of the externally applied electric field strength E in the shielded spatial afterglow. The bars around the data points do not represent an error, but rather the spread indicated by the one-sigma interval. Furthermore, the figure shows the combined data of 10 separate experiments (two for each value of E) consisting in total of 8623 particles.

4. Results charge control

In this section the proof of principle of the particle charge control technique is presented. Figure 8 shows the horizontal velocity v_x of the particles as a function of the external electric field strength E applied to the electrodes in the shielded spatial plasma afterglow. This figure shows that $v_x = 0 \, \text{mm s}^{-1}$ for $E = 0 \, \text{V m}^{-1}$, which is expected since the electric force—if present—is the dominant one in the horizontal direction. In addition, it shows that v_x is initially negative when a field is applied and becomes less negative with an increasing field strength, eventually even reaching a positive mean value. The sign of v_x is a direct indication of the particle charge sign. While a negative value of v_x corresponds to negatively charged particles, a positive value indicates that the particles are positively charged. It will be shown in section 5 that the vertical electric field between the mesh grid and the electrodes (see figure 3) has a key role in the charge control principle.

An upper estimate of the particle charge Q is shown in figure 9. This estimate is obtained by assuming that the measured horizontal velocity is solely caused by the integrated effect of the electric field created by the electrodes above the field of view (FoV). The FoV is indicated by the dashed lines in figure 2. This means that for the charge estimate it is assumed that the horizontal electric field strength above the electrodes is zero (between the electrodes and the mesh grid).

More specifically, the electric field strength between the electrodes but in the $y_t = 20 \, \text{mm}$ above the FoV (see figure 2) is taken to be constant with a magnitude equal to E in the centre of the electrodes. Using the vertical settling velocity ($v_{p,f} = 0.13 \, \text{m s}^{-1}$), the residence time of the particles is obtained $t_r = y_t/v_{p,f} = 0.15 \, \text{s}$. The particle charge in electrons can then be estimated using the simple formula $Q = v_x m_p/Et_r$, which originates from the assumption that the horizontal velocity is caused by a constant electric-field-driven acceleration during t_r. The upper estimate for the particle charge obtained this way is in accordance with the particle charge measured in the free spatial afterglow in our previous work [9].

Note that the bars around the data points in figures 8 and 9 do not represent an error, but rather the spread in v_x and Q (which is indicated by the one-sigma interval). It can be

disturbances are discussed in more detail in section 5.3. Therefore, the velocity was used for analysis of the particle charge instead of the acceleration.

To illustrate the difference between the particle trajectories measured in the free spatial afterglow [9] and the shielded spatial afterglow reported here, typical trajectories of both situations are shown in figure 6 in the case of the free afterglow and figure 7 in case of the shielded afterglow. It is clear that the acceleration of the trajectories in figure 7 is smaller than in figure 6. Independent of the charge, the strength of this measurement technique was the ability to simultaneously measure the individual charge of multiple particles as long as all particles were within the imaging region.

More details on the accuracy of this measurement technique were elaborated in our previous publication [9]. In that letter, it was also shown that mutual Coulomb interaction between the particles could be neglected due to the low particle density. In addition, it was shown that the afterglow plasma did not influence the electric field distribution at the position of the electrodes. These experiments were performed in the free spatial afterglow where the plasma density was higher than in the shielded spatial afterglow reported here. Therefore, it can be concluded that the afterglow plasma did not influence the field distribution at the position of the electrodes in this work.
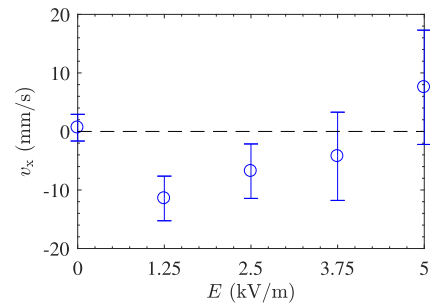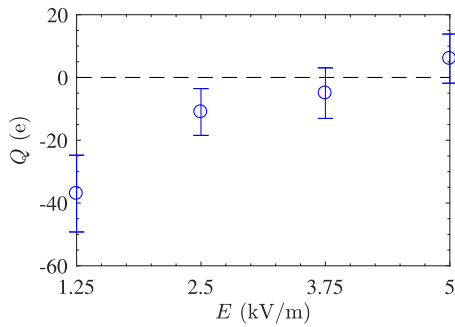
Figure 9. Upper estimate of the charge Q as a function of the externally applied electric field strength E in the shielded spatial afterglow. The bars around the data points do not represent an error, but rather the spread indicated by the one-sigma interval. Furthermore, the figure shows the combined data of 10 separate experiments (two for each value of E) consisting in total of 8623 particles.

observed that the spread in v_x increases with increasing magnitude of E whereas the spread in Q remains approximately constant, which is in accordance with expectation. For a higher electric strength, the deviations in electric force and consequently also the deviations in v_x are more distinct. The approximately constant spread in Q is not only caused by variations in particle size, leading to variations in charge and mass, but also by the stochastic nature of the plasma charging currents arriving at the particle surface [41]. These effects were discussed in more detail in our previous work [9].

The trends observed in v_x and Q as a function of E prove the ability to control the charge of the micro-particles in the PPCI setup by varying only the externally applied electric field strength. It will be shown in the next section that this can be explained by the local changes in ion density in the shielded spatial afterglow.

5. Physical interpretation

This section is dedicated to the interpretation of the physical processes that determine the presented charge control. In the following subsection arguments and results are discussed to explain and substantiate the proof of principle presented in section 4. These results are explained in three subsections corresponding to the three main regions which determine the charge of the micro-particles: the active plasma region, the sheath layer above the mesh grid and the shielded spatial plasma afterglow.

5.1. Active plasma region

In the active plasma region, the initial triboelectric charge distribution is reset and all particles reach an equilibrium charge which will be estimated here. Collisional effects will be briefly discussed as well.

In the quasineutral active plasma region, orbital motion limited (OML) theory (see section 2) can be applied to calculate the charge of the particles [8, 42]. For a typical electron temperature of $T_e = 1$ eV [43, 44], the charge acquired by the (4.9 ± 0.2) μm particles is around $Q_a = -5 \times 10^3 e$.

The plasma density in the active plasma region was measured using microwave interferometry (MWI) (see for more details section 3.2) and resulted in a typical value of $n_{e,i} = 10^{14}$ m^{-3}. Consequently, the charging timescale of the particles was in the order of microseconds (see equation (3)). Comparing this to the fact that the particles resided for several seconds in the active plasma region, it is concluded that all particles (assuming mono-dispersity) reached the same equilibrium charge independent of their initial triboelectric charge. Additionally, it should be mentioned that the dust particle density was sufficiently small to assume not only that the particles did not influence the plasma parameters, i.e. the so called Havnes parameter [45] is around 10^{-4}, but also that mutual Coulomb-interactions are negligible (see section 3.6).

5.2. Sheath above mesh grid

It is likely that the charge of the micro-particles, acquired in the active plasma region, changed drastically in the sheath layer above the mesh grid as in this region the free electron density is depleted. In the next paragraph, the effect of the dominated ion current over electron current on the particle charge will be estimated. In addition, the influence of possible particle scattering on the mesh grid will be treated in the remainder of this section.

The plasma-charged particles were partially decharged in the sheath region above the grounded mesh grid. To provide a first order estimate of this effect, the total ion current arriving at the surface of the particles is calculated, neglecting Coulomb interactions between the ions and the particle and assuming that the electron density is zero in this region. Using these assumptions the number of ions collected by a dust particle N_i was estimated by

$$N_i = \pi r_p^2 v_b n_i \tau_t \approx 10^3. \qquad (4)$$

Here, r_p is the radius of the particle, v_b the Bohm velocity and τ_t the transit time of the particle through the sheath region. The latter parameter is estimated by dividing the sheath size, taken to be 10 mm, by the settling velocity $v_{p,f} = 0.13$ m s^{-1}. Consequently, the particle charge decreased from the plasma bulk value ($Q_a = 5 \times 10^3 e$) in the sheath layer above the mesh grid to approximately $Q_s = -(10^2$ to $10^3)e$.

In addition to the local decharging, the particle were also influenced by an electric field strength in the sheath region above the mesh grid. Due to the orientation of the grid and the fact that the mesh grid size is much smaller than the sheath thickness, the electric field was mainly oriented in the vertical direction anti-parallel to the movement of the particles. Therefore, this vertical electric field did not influence the horizontal component of the trajectories measured between the electrodes.

Before the results of the shielded plasma afterglow are treated (section 5.3), the possible influence of particles scattering on the mesh grid is discussed. In figure 10, a histogram of the horizontal position x of the first detection of 9119 trajectories is shown both with plasma (in red) and without plasma (in blue). It can be observed that there are distinct peaks in the
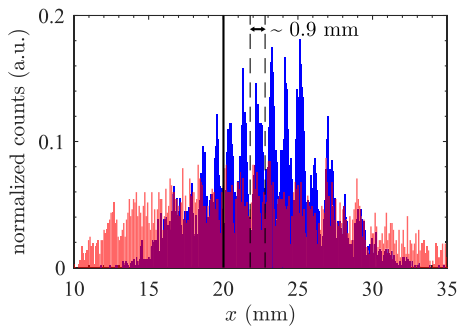
Figure 10. Histogram of the horizontal position x of the first detection of each trajectory for the situation without plasma (in blue) and with 6 W ICP (in red) for $E = 0\,\mathrm{V\,m^{-1}}$. The figure shows the combined data of three separate experiments for each configuration consisting in total of 7791 particles without plasma and 3909 particles with plasma. The solid vertical line at $x = 20$ mm indicates the axis of symmetry.

histograms at the positions where particles were blocked by the wires of the mesh grid.

It is concluded that there was no significant scattering of both the triboelectrically charged and plasma charged particles on the mesh grid and consequently it is assumed that there was no significant charge exchange between the particles and the mesh grid. Moreover, it is concluded that there was no flow turbulence to the extent that it influenced the particle trajectories. Heijmans and Nijdam [28] have shown that the triboelectric charge of 100 μm polystyrene particles can be as large as $\pm 5 \times 10^6 e$. This shows that the triboelectric particle charge can be of the same magnitude or even larger than the particle charge in the active plasma region.

Yet, the minima between the peaks in figure 10 are not zero. This could be caused by two factors. First of all, the mesh grid was not perfectly aligned with the laser sheet. Since the laser sheet was about 3 mm thick (see section 3.4), several rows of the mesh grid were imaged simultaneously. Consequently, overlapping peaks could have been created which could have resulted in non-zero minima. Second, the flow was compressed by the curved electrodes which means that the peaks were pushed together as well. This effect can also be seen in the distance between the peaks in figure 10 which is about 0.9 mm, significantly smaller than the expected separation distance of 1.5 mm (see mesh grid geometry section 3.2). The effect of the curved electrodes on the flow will be discussed extensively in section 5.3.

Upon comparison of the histograms of the particle density with and without plasma in figure 10, it is clear that the plasma causes the particles to be more spread out over at least the volume of the laser sheet. This increase in spread could be caused by the temperature gradient present in the argon flow. It is shown in previous studies that the neutral gas temperature in a low-pressure ICP strongly depends on the mode and can be elevated above room temperature [43, 46]. In addition, the increase in spread could be caused by the ion drag force pushing the particles to the walls of the glass tube.

Furthermore, it is clear that the local maxima of the distributions depicted in figure 10 are shifted. This could be caused

by the already mentioned flow compression effect and the horizontal temperature gradient since most of the particles passed through the right of the centre of the electrodes (the centre is at $x = 20$ mm in figure 10 as indicated by the vertical solid line). Moreover, also the global maxima of the distributions are shifted. The cause of this effect is uncertain because it is not known what the particle charge is in the situation where $E = 0\,\mathrm{V\,m^{-1}}$.

5.3. Shielded spatial plasma afterglow

In the previous sections the influences of the active plasma region and the sheath above the mesh grid were discussed. In these regions all particles reached a constant negative equilibrium charge independent of their initial triboelectrically charge. The actual control of the charge is achieved in the shielded spatial afterglow. In this section the governing mechanism is explained in detail.

First, the influence of the electrodes on the particle trajectories as well as the measured horizontal acceleration as a function of the electric field strength are discussed. Second, a current measurement is presented which shows that the ratio of n_i/n_e was actually changed by varying the electric field strength. Third, the magnitude of the ion drag is estimated and it is concluded that this force is negligible and thereby did not contribute to the observed phenomena. Finally, it is shown that ions were focussed on the cathode and thereby created an asymmetric spatial charge distribution.

5.3.1. Acceleration at the electrodes. The curved electrodes that were used to generate the electric field had a separation distance of 40 mm (see section 3.3) whereas the tube had an inner width of 0.1 m. Consequently, the flow was compressed at this position, which influenced the particle trajectories. In figure 11 the horizontal velocity v_x is shown and in figure 12 the horizontal acceleration a_x for the situation without plasma and $E = 0\,\mathrm{V\,m^{-1}}$. As expected, for most particles the initial velocity was directed towards the centre of the tube, positive for $x \lesssim 20$ mm and negative for $x \gtrsim 20$ mm, while the acceleration was directed outwards, negative for $x \lesssim 20$ mm and positive for $x \gtrsim 20$ mm. Yet, some particles had a velocity directed away from the centre of the tube. This can be explained by the fact that some particles were detected for the first time below the symmetry axis of the electrodes (see figure 2), where the flow was spreading out again.

In figure 13 the horizontal acceleration is shown as a function of the electric field strength E. While the measured acceleration provides information about the local charge between the electrodes, the horizontal velocity provides information about the charge in a larger region of the shielded spatial afterglow through the integrated effect of the electric field above and between the electrodes. Consequently, the integrated trend of the particle charge is better observed in the velocity which is therefore used in the analysis of the charge control.

5.3.2. Current received by electrodes. A key point when it comes to charge control is the confirmation that the presence of the mesh grid and the electrodes attracted ions from
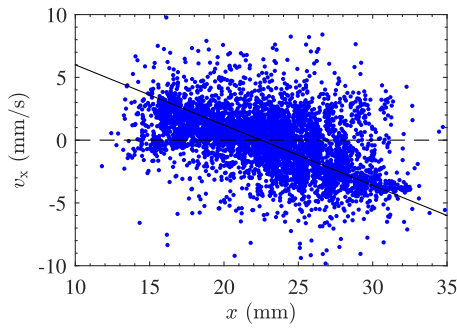
Figure 11. Scatter plot of the horizontal velocity v_x as a function of the first x position for the case without plasma and $E = 0\,\mathrm{V\,m^{-1}}$. The figure shows the combined data of three separate experiments consisting in total of 7791 particles. A solid line is added to illustrate the v_x dependence on x and a dashed line to indicate the zero-crossing.

Figure 12. Scatter plot of the horizontal acceleration a_x as a function of the first x position for the case without plasma and $E = 0\,\mathrm{V\,m^{-1}}$. The figure shows the combined data of three separate experiments consisting in total of 7791 particles. A solid line is added to illustrate the a_x dependence on x and a dashed line to indicate the zero-crossing.
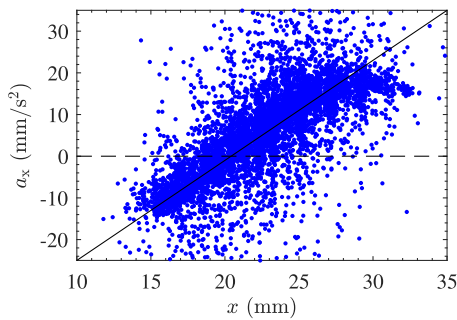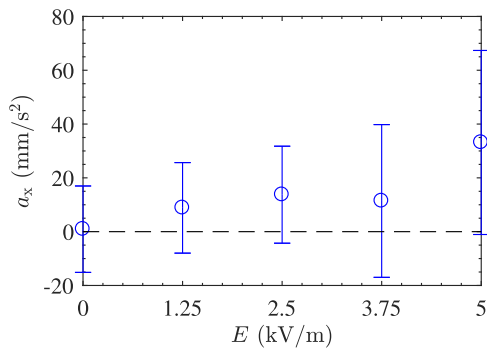

Figure 13. Horizontal acceleration a_x as a function of the externally applied electric field strength E in the shielded spatial afterglow. The figure shows the combined data of 10 separate experiments (two for each value of E) consisting in total of 8623 particles.

the sheath above the mesh grid into the shielded spatial afterglow. In fact, the mesh grid caused the ions to be focussed in the region below. This effect is well known in literature and is extensively used for plasma-based ion sources [47, 48]. More specifically, the chosen geometry created a vertical dc electric field between the electrodes and the grounded mesh grid
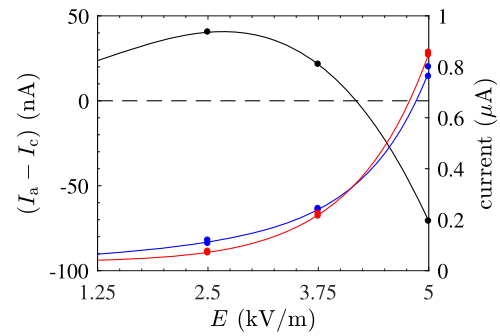

Figure 14. In black, the difference between the anode and the cathode current as a function of the applied electric field strength E. In addition, the individual anode and cathode current are plotted in blue and red, respectively. For each value of E the current has been measured twice in separate experiments which is indicated by two points for both currents at each E value in the plot. Fit curves are solely added in the figure to guide the eye.

(see figure 3). This vertical electric field most likely attracted ions from the sheath into the shielded spatial afterglow. Due to presence of the horizontal field between the electrodes, the plasma species likely gained a non-uniform spatial distribution in horizontal direction. In order to substantiate this statement, the current going to both electrodes was measured separately in a floating configuration (see section 3.3) and the results are shown in figure 14.

It is clear from this graph that the anode current exceeds the cathode current up to a field strength of approximately $4.5\,\mathrm{kV\,m^{-1}}$, after which the cathode current exceeds the anode current. This trend matches the observed trend in horizontal velocity as a function of E (see figure 8). Assuming that the anode current is mostly caused by the electrons and the cathode current by ions, figure 14 indicates that the local ion density is responsible for the charge control of the microparticles. In addition, it can be observed that the anode and cathode current are of the same order of magnitude. Yet, the electron velocity is much larger than the ion velocity, even if both electrons and ions were approximately at room temperature. Thus, assuming that both electrons and ions were collected by the total area of the electrodes, which is a first order estimate, the ion density likely dominates the electron density according to $n_i/n_e \approx v_e/v_i \propto m_i/m_e$, where m_e is the electron mass.

The ion density is estimated under the presented assumptions using $n_i = I_c/A v_{d,i} e = 10^{11}\,\mathrm{m^{-3}}$. Here, A is the cathode surface area and $v_{d,i}$ the ion drift velocity. For the estimation of n_i the cathode current at $E = 1\,\mathrm{kV\,m^{-1}}$ is used. The estimated ion density of $n_i = 10^{11}\,\mathrm{m^{-3}}$ means that the linearised Debye length is in the sub cm range and is the same order of magnitude as the diffusion length [49, 50], which is given by $D/2\pi \approx 2$ cm, assuming an infinitely long square beam. Hence, the interaction strength between ions and electrons is decreased and thus the plasma species are no longer bound by ambipolar diffusion [51, 52]. This in turn alters the electron and ion current arriving at the particle surface and consequently the particle charge. As stated in the introduction, Couëdel *et al* [14] have shown that the manner in which the transition from
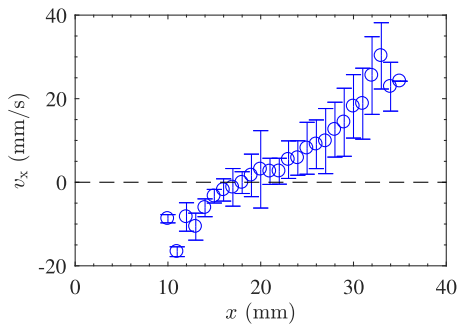
Figure 15. Horizontal velocity v_x as a function of the first x position for $E = 5\,\text{kV}\,\text{m}^{-1}$ and a plasma power of 6 W. The figure shows the combined data of two separate experiments consisting in total of 1244 particles. The corresponding data is averaged in spatial bins of 1 mm in size.

ambipolar to free diffusion takes place influences the particle charge. Overall, the current measurement presented here confirmed our earlier statement that an electric field-induced altering of the local ion density is responsible for the charge control.

5.3.3. Ion drag. It has been shown in the previous section that ions dominate the shielded spatial afterglow region. Therefore, the possible influence of the ion drag force on the horizontal velocity is discussed. For 0.9 mbar argon the ion drag force is described by the linear plasma response formalism which takes into account ion-neutral collisions. However, ion absorption at the particle surface is neglected [1, 53]. Using the formalism for a flowing plasma [54], the electric field-induced velocity component of the ions is included in the estimate of the ion drag. First of all, it can be concluded that the ion drag force is about a factor 10 smaller than the electric force on a micro-particle with a charge of i.e. when $n_e < 1 \times 10^{13}\,\text{m}^{-3}$ and assuming $T_e < 1\,\text{eV}$ and $E = 1\,\text{kV}\,\text{m}^{-1}$. Secondly, it can be concluded that according to the linear plasma response formalism the ion drag force scales linearly with the ion velocity and can consequently not explain the measured change in v_x as a function of E. Hence, these two arguments show that the ion drag force is negligible in the shielded plasma afterglow.

5.3.4. Asymmetric ion distribution. If free ions and electrons were present in the shielded spatial afterglow, it would be expected that these free charge carriers were non-uniformly distributed between the electrodes in the presence of an electric field. Therefore, the charge of the particles, and consequently their velocity, should also depend on their position. This very effect can be observed in figure 15, where the mean value and standard deviation of v_x are plotted for all positions with the data grouped in spatial bins of 1 mm. It is clear that the velocity has a maximum negative value close to the anode and increases as the distance to this electrode is increased, eventually becoming positive near the cathode. This situation corresponds to the expected distribution of charge carriers, namely more electrons at the anode and more ions at the cathode. Consequently, the particles experienced an increased positive ion flux near the cathode, while they remained negatively charged close to

the anode. In conclusion, the asymmetric velocity distribution excellently corroborates that a free positive space charge in the shielded spatial afterglow is the dominant reason for the observed charge control.

6. Conclusion

In this paper, we have shown that the charge of micro-particles can be controlled by shielding the spatial afterglow from the bulk plasma by the application of a mesh grid and by changing an externally applied electric field strength below this mesh grid. In this manner, the particle charge has been controlled from small negative charges to small positive charges, typically in the range of $Q = \pm 10e$, by varying the local ion space charge distribution in the shielded spatial afterglow. The governing mechanism for this variation in ion density is the vertical electric field component arising from the geometry of the setup. These variations in ion density have been confirmed by measurement of the separate currents received by each of the electrodes, which generated the external electric field, and by the asymmetric distribution of the horizontal velocity v_x as a function of the horizontal distance x. The strength of the reported technique is that the actual control is achieved in the shielded spatial afterglow, while the particles reached a constant equilibrium charge in the other regions above the mesh grid.

The achieved control of the particle charge not only opens up ways to study nano-scale surface charging physics on micro-meter length scales and fundamental plasma plasma-particle interactions. The insights obtained in this work also contribute to the further development of plasma-assisted contamination control strategies.

ORCID iDs

B van Minderhout https://orcid.org/0000-0002-6398-9704
J C A van Huijstee https://orcid.org/0000-0001-8181-3414
B Platier https://orcid.org/0000-0003-4524-0131
J Beckers https://orcid.org/0000-0001-6116-7013

References

[1] Khrapak S and Morfill G 2009 *Contrib. Plasma Phys.* **49** 148
[2] Beckers J, Trienekens D J M and Kroesen G M W 2013 *Phys. Rev.* E **88** 1
[3] Chaudhuri M, Khrapak S A, Kompaneets R and Morfill G E 2010 *IEEE Trans. Plasma Sci.* **38** 818

[4] Morfill G E, Annaratone B M, Bryant P, Ivlev A V, Thomas H M, Zuzic M and Fortov V E 2002 *Plasma Phys. Control. Fusion* **44** 263

[5] Vollath D 2008 *J. Nanopart. Res.* **10** 39

[6] Van De Wetering F M, Brooimans R J, Nijdam S, Beckers J and Kroesen G M 2015 *J. Phys. D: Appl. Phys.* **48** 35204

[7] Beckers J, Stoffels W W and Kroesen G M 2009 *J. Phys. D: Appl. Phys.* **42** 155206

[8] Tang X and Delzanno G 2014 *Phys. Plasmas* **21** 123708

[9] Van Minderhout B, Peijnenburg T, Blom P, Vogels J M, Kroesen G M and Beckers J 2019 *J. Phys. D: Appl. Phys.* **52** 32LT03

[10] Ivlev A V *et al* 2003 *Phys. Rev. Lett.* **90** 55003

[11] Couëdel L, Mikikian M, Boufendi L and Samarian A A 2006 *Phys. Rev. E* **74** 026403

[12] Couëdel L, Mezeghrane A, James B, Mikikian M, Samarian A, Cavarroc M, Tessier Y and Boufendi L 2007 *ECA* **31F** P2.068

[13] Couëdel L, Samarian A A, Mikikian M and Boufendi L 2008 *Europhys. Lett.* **84** 35002

[14] Couëdel L, Samarian A A, Mikikian M and Boufendi L 2008 *Phys. Plasmas* **15** 063705

[15] Couëdel L, Mezeghrane A, Samarian A A, Mikikian M, Tessier Y, Cavarroc M and Boufendi L 2009 *Contrib. Plasma Phys.* **49** 235

[16] Filatova I I, Trukhachev F M and Chubrik N I 2011 *Plasma Phys. Rep.* **37** 1042

[17] Layden B, Couëdel L, Samarian A A and Boufendi L 2011 *IEEE Trans. Plasma Sci.* **39** 2764

[18] Wörner L *et al* 2013 *Phys. Plasmas* **20** 10

[19] Land V and Goedheer W J 2007 *IEEE Trans. Plasma Sci.* **35** 280

[20] Bagheri B *et al* 2018 *Plasma Sources Sci. Technol.* **27** 15

[21] Hoppel W A 1985 *J. Geophys. Res. Atmos.* **90** 5917

[22] Romay F J and Pui D Y 1992 *J. Aerosol Sci.* **23** 679

[23] Stefanović I, Berndt J, Marić D, Šamara V, Radmilović-Radjenović M, Petrović Z L, Kovačević E and Winter J 2006 *Phys. Rev. E* **74** 1

[24] Boufendi L, Jouanny M C, Kovacevic E, Berndt J and Mikikian M 2011 *J. Phys. D: Appl. Phys.* **44** 174035

[25] Martin Knotter D and Wali F 2010 *Dev. Surf. Contam. Clean. Part. Depos. Control Remov.* 1st edn (Amsterdam: Elsevier Inc.) pp 81–120

[26] Beckers J, Ockenga T, Wolter M, Stoffels W W, Van Dijk J, Kersten H and Kroesen G M 2011 *Phys. Rev. Lett.* **106** 115002

[27] Lee V, Waitukaitis S R, Miskin M Z and Jaeger H M 2015 *Nat. Phys.* **11** 733

[28] Heijmans L C J and Nijdam S 2016 *Europhys. Lett.* **114** 64004

[29] Bennet E D *et al* 2016 *J. Aerosol Sci.* **100** 53

[30] Thoma M H *et al* 2007 *IEEE Trans. Plasma Sci.* **35** 255

[31] Antonova T, Khrapak S A, Pustylnik M Y, Rubin-Zuzic M, Thomas H M, Lipaev A M, Usachev A D, Molotkov V I and Thoma M H 2019 *Phys. Plasmas* **26** 113703

[32] Kennedy R V and Allen J E 2003 *J. Plasma Phys.* **69** 485

[33] Whipple E C 1981 *Rep. Prog. Phys.* **44** 1197

[34] Khrapak S A, Morfill G E, Khrapak A G and D'Yachkov L G 2006 *Phys. Plasmas* **13** 052114

[35] Bouchoule A 1999 *Dusty Plasmas: Physics, Chemistry and Technological Impacts in Plasma Processing* (New York: Wiley Inc.) pp 1–27

[36] Rogowski W 1923 *Arch. Elektrotech.* **12** 1–15

[37] Schepers L P T, IJzerman W L and Beckers J 2018 *J. Phys. D: Appl. Phys.* **51** 375203

[38] Sikimić B, Stefanović I, Denysenko I B, Winter J and Sadeghi N 2014 *Plasma Sources Sci. Technol.* **23** 025010

[39] Sikimić B, Stefanović I, Denysenko I B and Winter J 2013 *Plasma Sources Sci. Technol.* **22** 045009

[40] Zhang X, Zhang Z K, Cao J X, Liu Y and Yu P C 2018 *AIP Adv.* **8** 035121

[41] Khrapak S A, Nefedov A P, Petrov O F and Vaulina O S 1999 *Phys. Rev. E* **59** 6017

[42] Bacharis M, Coppins M and Allen J E 2010 *Plasma Sources Sci. Technol.* **19** 025002

[43] Godyak V A, Piejak R B and Alexandrovich B M 2002 *Plasma Sources Sci. Technol.* **11** 525

[44] Lieberman M A and Lichtenberg A J 2005 *Principles of Plasma Discharges and Materials Processing* 2nd edn (New York: Wiley Interscience) pp 1–757

[45] Samarian A A and Vladimirov S V 2003 *Phys. Rev. E* **67** 5

[46] Poirier J S, Bérubé P M, Margot J, Chaker M and Stafford L 2009 *29th ICPIG* vol 10

[47] Aston G and Wilbur P J 1981 *J. Appl. Phys.* **52** 2614

[48] Loeb H W 2005 *Plasma Phys. Control. Fusion* **47** B565

[49] Luikov A 1968 *Analytical Heat Diffusion Theory* 2nd edn (New York: Academic)

[50] Makabe T and Petrovic Z L 2015 *Plasma Electronics: Applications in Microelectronic Device Fabrication* 2nd edn (Boca Raton, FL: CRC Press, Taylor & Francis Group)

[51] Gerber R A and Gerardo J B 1973 *Phys. Rev. A* **7** 781

[52] Platier B, Limpens R, Lassise A C, Staps T J, Van Ninhuijs M A, Daamen K A, Luiten O J, Ijzerman W L and Beckers J 2020 *Appl. Phys. Lett.* **116** 103703

[53] Khrapak S A, Chaudhuri M and Morfill G E 2009 *IEEE Trans. Plasma Sci.* **37** 487

[54] Ivlev A V, Khrapak S A, Zhdanov S K, Morfill G E and Joyce G 2004 *Phys. Rev. Lett.* **92** 1